Article

First Experimental Demonstration of the Wide-Field Amplitude Surface Plasmon Resonance Microscopy in the Terahertz Range

Vasiliy Valerievich Gerasimov [1,2,*] **, Oleg Eduardovich Kameshkov** [1,2] **, Alexey Konstantinovich Nikitin** [3] **, Ildus Shevketovich Khasanov** [3,*] **, Alexey Georgievich Lemzyakov** [1] **, Irina Veniaminovna Antonova** [4,5,6] **, Artem Ilyich Ivanov** [4,6] **, Nghiem Thi Ha Lien** [7] **, Nguyen Trong Nghia** [7] **, Le Tu Anh** [8] **, Nguyen Quoc Hung** [9] **and Ta Thu Trang** [10]

1   Budker Institute of Nuclear Physics, Siberian Branch of the Russian Academy of Sciences, 11, Lavrentiev Prospect, 630090 Novosibirsk, Russia; o.kameshkov@g.nsu.ru (O.E.K.); a.g.lemzyakov@inp.nsk.su (A.G.L.)
2   Department of Physics, Novosibirsk State University, 630090 Novosibirsk, Russia
3   Scientific and Technological Centre of Unique Instrumentation of RAS, 15, Bytlerova Street, 117342 Moscow, Russia; alnikitin@mail.ru
4   Rzhanov Institute of Semiconductor Physics SB RAS, 13 Lavrentiev Aven., 630090 Novosibirsk, Russia; antonova@isp.nsc.ru (I.V.A.); art.iv.il@mail.ru (A.I.I.)
5   Department of Semiconductor Devices and Microelectronics, Novosibirsk State Technical University, 20 K. Marx Str., 630073 Novosibirsk, Russia
6   Department of Physics, Siberian State University of Telecommunications and Information Science, 86 Kirov Str., 630102 Novosibirsk, Russia
7   Institute of Physics, Vietnam Academy of Science and Technology, 10, Daotan, Badinh, Hanoi 11935, Vietnam; halien@iop.vast.vn (N.T.H.L.); trongnghia@iop.vast.vn (N.T.N.)
8   Vietnam Academy of Science and Technology, University of Science and Technology of Hanoi, 18 Hoang Quoc Viet, Cau Giay, Hanoi 11307, Vietnam; anhlt.bi11-013@st.usth.edu.vn
9   Nano and Energy Center, VNU University of Science, Vietnam National University, 334, Nguyen Trai, Thanh Xuan, Hanoi 11935, Vietnam; hungngq@hus.edu.vn
10   Joint Vietnam-Russia Tropical Science and Technology Research Center, Institute of Tropical Durability, 63 Nguyen Van Huyen, Cau Giay District, Hanoi 11307, Vietnam; ntthuy@iop.vast.vn
*   Correspondence: v.v.gerasimov@inp.nsk.su (V.V.G.); khasanov@ntcup.ru (I.S.K.)

Abstract: We have demonstrated the wide-field amplitude surface plasmon resonance (SPR) microscopy technique in the terahertz (THz) range. A Zeonex polymer prism was utilized to excite surface plasmon polaritons (SPPs) through attenuated total reflection (ATR) in an Otto configuration. Coherent quasimonochromatic radiation with a wavelength of approximately 197 μm, generated by the Novosibirsk free electron laser, was employed. Our results indicate that the SPR microscopy method is applicable for investigating the planar surfaces of semiconductors at THz frequencies, provided that the SPPs' cutoff frequency is close to the probing radiation frequency. This condition ensures that the propagation length of the SPPs is comparable to the radiation wavelength. By varying the air gap between the prism and the surface under examination, we acquired images of a polypropylene coating 20 μm thick and a graphene coating 35 nm thick on a flat indium antimonide substrate. The boundary between the coated and uncoated regions can be precisely localized through determination of the kink in the reflection coefficient of the THz radiation beam that illuminates the boundary between the regions if the optimal conditions for the generation of the SPPs in the uncoated region are met.

Keywords: surface plasmon polaritons; terahertz microscopy; indium antimonide; graphene films

1. Introduction

Terahertz (THz) microscopy is a promising tool for various research fields, including materials science [1], biology [2], medicine [3], and nondestructive testing [4]. THz

microscopy offers advantages over traditional optical microscopy as the radiation can penetrate materials opaque to visible light, while being non-ionizing and low-energy and, thus, safe for delicate samples, such as works of art [5]. Additionally, THz radiation interacts with chemical bonds and functional groups, enabling the visualization of chemical and structural changes in substances such as polymers and biomolecules [6,7].

However, THz microscopy faces challenges because the size of the structures in the studied materials is typically smaller than the THz wavelength. This limitation leads to low sensitivity and resolution. To overcome these limitations, various approaches have been developed for achieving super-resolution, such as THz scanning near-field optical microscopy (THz-SNOM) [8], THz solid immersion microscopy [9], deconvolution techniques [10], structured illumination [11], ghost imaging [12], and others. Although scanning methods offer high resolution and sensitivity, they suffer from drawbacks, such as low scanning speed, and difficulties in investigating heterogeneous samples. Wide-field methods, on the other hand, operate in the far wave zone, which is advantageous for nondestructive testing and allows the use of multipixel cameras, which speeds up the measurement process.

As for the study of thin objects on flat surfaces, particularly in microscopy, methods utilizing surface electromagnetic waves (SEW) have shown promise [13]. Among these, surface plasmon resonance (SPR) microscopy [14,15] utilizes surface plasmon polaritons (SPPs)—a special type of SEW—excited at the interface between materials, with different dielectric permittivity signs [16]. SPR microscopy [17] combines the benefits of optical microscopy, such as measurements in atmospheric conditions, equipment affordability, and the ability to study low-contrast thin-layer objects, with the high vertical resolution of the microscopy at the interface and its transition layer. SPPs have an upper cutoff frequency defined by the plasma frequency ω_p, beyond which only bulk plasmon polaritons can be excited. Below ω_p (more accurately, $\omega_p/\sqrt{2}$ in air), only SPPs can exist [18].

Various configurations have been proposed to observe the SPP phenomenon, including gratings [19,20], waveguide [21], and prism coupling [22,23]. The prism methods, particularly the Otto configuration (for opaque samples with an air gap not exceeding the depth of the SPP field penetration into air), and the Kretschmann configuration (for partially transparent samples applied to the prism base), are most suitable for wide-field SPR microscopy. In the THz region, the Otto scheme exhibits advantages [24], allowing for the adjustment of the gap size without damaging the sample's surface. Bright-field microscopy is employed with a recording of the radiation reflected from the prism base. There are two types of SPR microscopy: amplitude and phase microscopy [25]. Phase microscopy relies on the observed phase shift, proportional to the object's refractive index, with a sharp phase jump occurring at the object's boundary, enabling a high boundary contrast. Amplitude microscopy records intensity changes, relating to the interference, scattering, and absorption phenomena in the object. These methods can be complementary, but amplitude microscopy is simpler to implement, requiring no interferometric techniques for phase determination and being less susceptible to noise (less sensitive to the surface roughness compared to phase microscopy). Thus, for the initial experiments in THz SPR microscopy, amplitude wide-field microscopy is the most suitable choice.

The objective of this study was to showcase the feasibility of implementing SPR microscopy in the THz range. We report the findings of the preliminary experiments conducted on a terahertz (THz) SPR microscopy in the Otto configuration. The experiments utilized indium antimonide as the substrate material and THz radiation from the Novosibirsk free electron laser. The choice of a semiconductor surface instead of metal is due to the propagation length of SPPs, comparable to the radiation wavelength [26].

2. Materials and Methods

To demonstrate the capabilities of wide-field SPR microscopy in the Otto geometry, an experimental setup was assembled according to the scheme presented in Figure 1. The Novosibirsk free electron laser [27] was used as the source of the THz radiation. Collimated

linearly polarized quasimonochromatic radiation with a central wavelength $\lambda c \approx 197$ μm (Figure 2) and average power of about 1 W fell on a thin-film polypropylene beam splitter; the reflected beam was recorded using the laser power meter IMO-4S (for control of the FEL power) and the passed beam fell on a rectangular prism made of polymer Zeonex (n ≈ 1.5), transparent in the THz and visible ranges. In the prism, the THz radiation fell on its base at an angle θ greater than the critical angle θ_{cr}. The relation between θ and the angle of incidence on the side face of the prism θ_{ext} is defined by the ratio $\theta = 45° - \arcsin(\sin(45° - \theta_{ext})/n)$. The intensity distribution in the beam's output from the prism was recorded using the pyroelectric focal plane array Pyrocam-IV (Pyroelectric FPA) with a 25×25 mm^2 (320×320 pixels) receiving area.

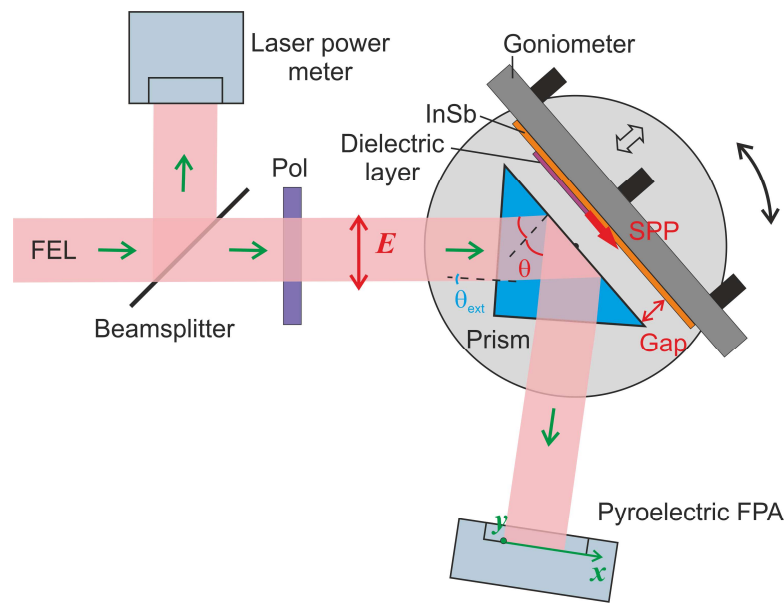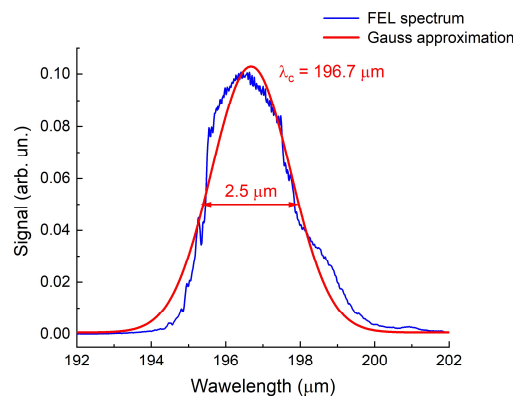**Figure 1.** Experimental setup.

Figure 2. Free electron laser radiation spectrum measured with a diffraction grating monochromator.

A polished plane-parallel plate of high-purity indium antimonide (InSb), attached to a high stability optics mount, was brought to the prism axis at a distance δ. The diameter of the plate was 50 mm and its thickness was 1 mm. At certain values of the incidence angle $\theta > \theta_{cr}$ and gap δ, surface plasmon polaritons (SPPs), the direction of spread of which is shown with the red arrow in Figure 1, were excited on the InSb surface, which reduced the intensity of the reflected beam. The parallelism of the prism base and the InSb plate was adjusted with the goniometer, and the gap δ was controlled by means of the linear motorized stage (Standa), which was moved with a step of 83 nm. The prism and optics mount with the InSb plate were mounted on a motorized translation stage, able to change

the angle θ with increments of 0.01°. The setup was adjusted according to the red beam of the diode laser, combined with the THz beam. The accuracy of setting the zero angle after adjustment was at least 0.1°.

Excitation of surface plasmon resonance (SPR) is possible only in a *p*-polarized (relative to the surface of the sample) radiation. For this reason, to reduce the parasitic background, a lithographic polarizer (Pol) was placed at the input of the setup, which cut off the *s*-component of the THz radiation.

3. Results and Discussion

To demonstrate and explore the capabilities of the SPR microscopy in the THz range, we conducted a series of experiments with three samples: a substrate of pure InSb (as a reference sample); an InSb substrate covered with polypropylene film 20 μm thick, transparent for THz radiation; and an InSb substrate with graphene layers.

### 3.1. Experiments with Free Surface of InSb

In order to determine the optimum value of the gap δ for the generation of the SPPs, we measured the dependence of the reflectance coefficient (in power) R on δ. For this purpose, at each gap, δ signals from all pixels of the receiving matrix were summed and then the sum of their background illumination was deducted from this sum; the resulting difference was normalized to the maximum integral signal from all pixels, recorded after the prism base was removed from the SPPs' field.

Figure 3 shows, as an example, images of the THz beam from the prism (diameter about 10 mm), taken by the pyroelectric FPA at the incidence angle θ = 42.1° and the different values of the gap δ between the prism and InSb plate. It can be seen that as δ grows (from its zero value), the intensity of the beam decreases, reaches the minimum, and then increases. Similar images were also obtained with θ = 44.6 and 41.6°.
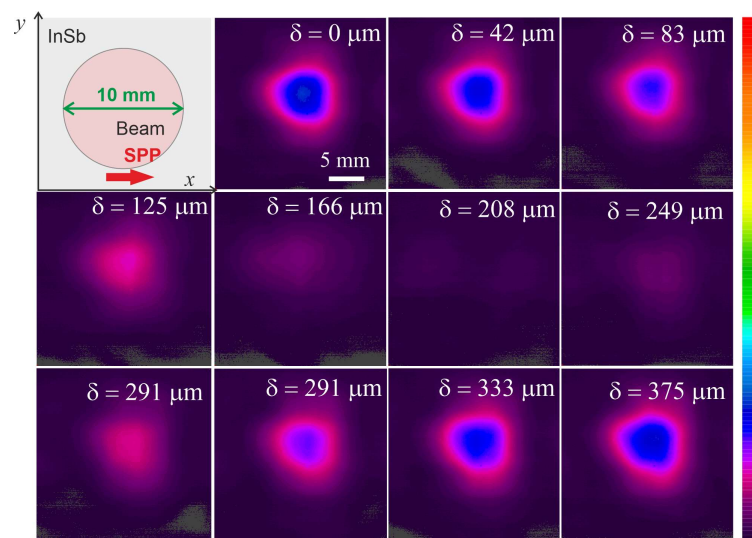
Figure 3. Images of the reflected THz beams vs. gap size δ, measured at the optimal incidence angle θ equal to 42.1°.

Figure 4 presents the $R(\delta)$ dependencies obtained at the three selected incidence angles θ. It can be seen that the depth of the dip, proportional to the efficiency of the plasmon resonance, depends on the incidence angle of the radiation. At θ = 42.1° and δ = 208 μm, the intensity of the THz radiation reflected from the prism base is close to zero, which indicates the fact that almost all the energy of the incident radiation is converted into the energy of the SPPs' field. Further experiments were carried out with the optimum incidence angle θ = 42.1°.
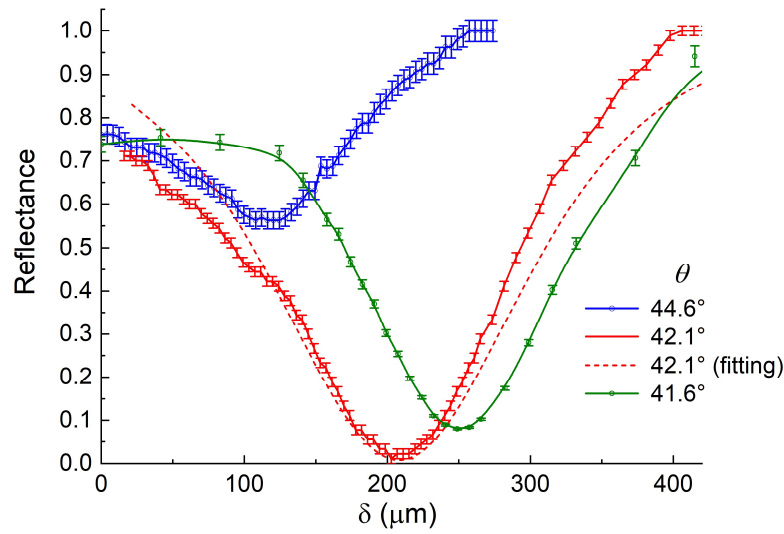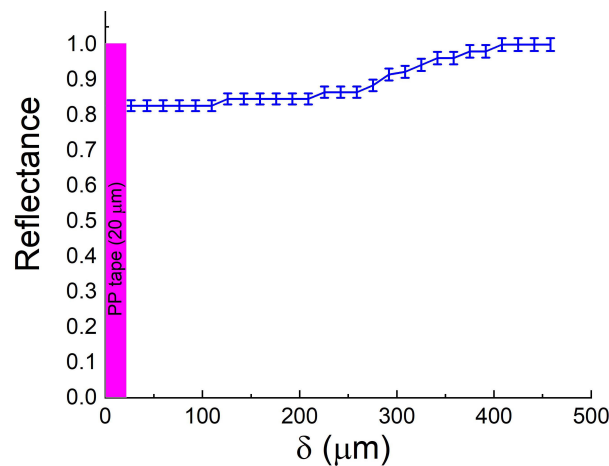
Figure 4. Reflectance vs. gap δ between the Zeonex ATR prism and the surface of the InSb sample, measured at different angles of incidence θ of the THz radiation on the prism base.

To estimate the unknown complex dielectric permittivity ε for InSb, we used the least squares method, comparing the experimental red curve (Figure 4) corresponding to the highest efficiency of the SPPs' excitation with the optical model of the prism-air-InSb multilayer structure, constructed using the transfer matrix method [28]. The InSb dielectric permittivity was found to be $\varepsilon = -18.52 + 3.03i$ at $\lambda = 197$ μm. Hence, the tangential component of the SPP wave vector on the free surface of InSb $k_x = \frac{2\pi}{\lambda}\sqrt{\frac{\varepsilon}{1+\varepsilon}} = 327.7 + 1.49i$ cm^{-1}, which corresponds to the SPP propagation length $L_{SPP} = \frac{1}{2k_x''} = 3.4$ mm $\approx 20\,\lambda$. The L_{SPP} value determines the lateral resolution of the SPR microscopy, which is significantly worse than the diffraction limit because the selected radiation frequency differs quite significantly from the SPPs' upper cutoff frequency for this semiconductor sample.

3.2. Localization of Polypropylene Film on the InSb Surface

When only part of the InSb surface with the polypropylene (PP) film 20 μm thick was illuminated by the THz radiation through the prism, the effectiveness of the SPR decreased dramatically, as evidenced by the virtual disappearance of the resonance dip in the $R(\delta)$ dependence (Figure 5). We used this effect to demonstrate the possibility of implementing SPR microscopy in the THz range.

Figure 5. Reflectance vs. gap size δ between the ATR prism and the surface of the InSb plate covered with 20 μm polypropylene tape, measured at the resonance incident angle θ = 42.1°.

To this end, we applied the PP film only on part of the InSb plate in such a way that its boundary was perpendicular to the radiation incidence plane (i.e., perpendicular to the direction of propagation of the SPPs); the rest of the surface of the plate remained free of coating. After directing the THz beam to the prism base area, comprising the edge of the PP film, we recorded the images of the beam from the prism at different values of the gap δ (Figure 6). We distinguished two zones on the matrix: zone A, in the part of the beam reflected from the free surface of the InSb, and zone B, in the part of the beam reflected from the film-covered area of the surface of the InSb. The boundary between the zones in Figure 6 is marked with the vertical dotted line.
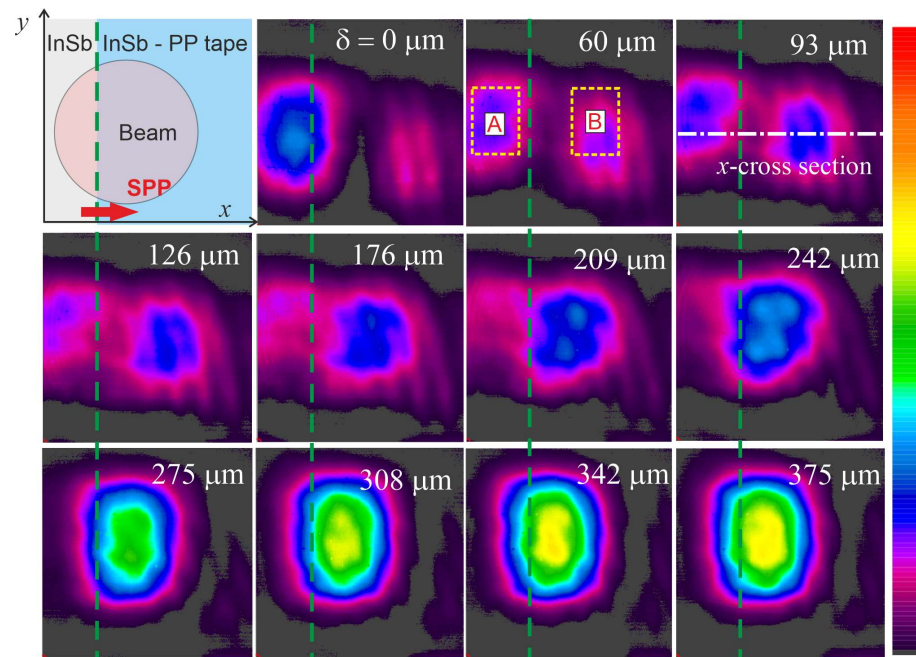

Figure 6. Images of reflected beams vs. gaps δ, measured for the InSb plate, half of which was covered with polypropylene scotch tape 20 μm thick. The angle of incidence θ was 42.1°.

At a small δ = 0−60 μm, the signal was significantly attenuated in both zones. For zone A, this attenuation is due to the Fresnel reflection from the prism–InSb boundary. For zone B (covered by the film), the radiation reflected from the prism base was not only significantly attenuated, but there were also interference bands observed against the background of this part of the attenuated reflected beam. In our opinion, the reason is that due to the small gap ($\delta < \lambda$) and the closeness of the film refraction index to the prism refraction index (n ≈ 1.5), the total internal reflection does not occur in these conditions. In this case, the wave falling on the prism base penetrates into the film and is reflected from the semiconductor's surface. The beams reflected from the base of the prism and both borders of the film have a path difference and interfere. Since the PP film is quite thick (20 μm), the path difference, even at a zero gap and taking into account the refractive index of the film, was about 60 μm (≈0.3 λ), which could cause a noticeable attenuation of the reflected beam.

As the gap increases (δ >60 μm), the intensity of the reflected radiation in zone A (without the PP film) decreases even further, due to the generation of SPPs, whereas in zone B (with the PP film), it increases; because at such gaps, the wave weakly tunnels through the film. At δ ≈ 210 μm, which corresponds to the most effective surface plasmon resonance, the intensity of the reflected radiation in zone A is minimal, and it remains high in zone B (see Figure 6). At δ > 270 μm, the evanescent wave formed in the air gap at the attenuated total internal reflection (ATR) is almost not reaching the semiconductor's surface, and the THz beam's intensity profile is identical to that of the corresponding parts

of the incident beam. The THz beam is completely reflected in both areas, its intensity profile being identical to the intensity profile of the incident beam.

To analyze the images shown in Figure 6, we constructed the intensity profiles of cross-sections of these images along the *x*-axis versus the gap δ (Figure 7). The scale on the *x*-axis is enlarged in accordance with the prism inclination angle relative to the incident beam ($1/\cos(\theta)$-fold enlargement). Interpretation of the resulting distributions is complicated by the interference effects mentioned above. At a zero gap δ, the profile has two maximums: the left one corresponds to the free InSb surface part (zone A) and is caused by the ATR phenomenon; the right maximum, corresponds to the part with the PP film (zone B), and is due to abovementioned interference effects. As δ increases, the left maximum decreases due to the generation of SPPs on the free InSb surface; the right maximum grows due to the weakening of the destructive interference. In addition, we can note a significant bias of the maxima relative to the profile of the incident beam (at δ = 325 μm).
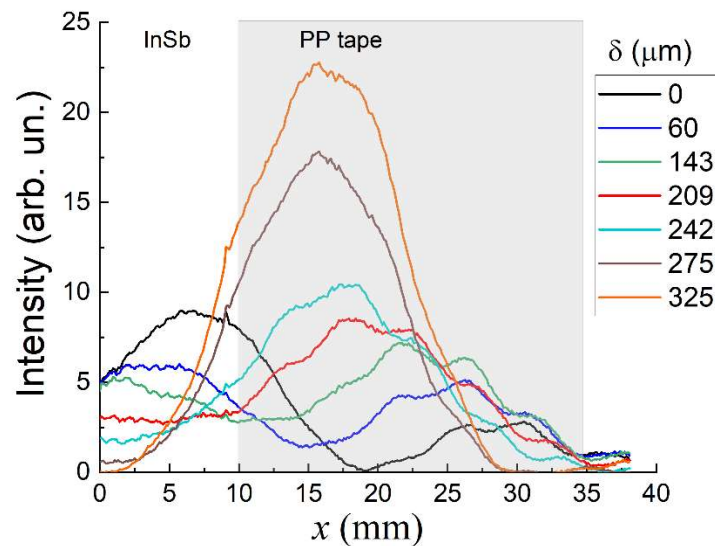
Figure 7. Cross-sections of the intensity profiles (see dashed line in Figure 6) along the *x*-direction at different air gaps δ.

To interpret this effect, let us consider a model example for a dielectric step on a conductive surface, observed under SPR conditions (Figure 8a). This example was considered in [29] for a plane wave. The reflected field can be described with an equation of the form $D(x) = E(x) \cdot r_{21} + D^+(x)$, where *x* is the coordinate on the surface (the boundary between the free surface ($x < 0$)) and the dielectric film ($x > 0$) is at $x = 0$, $E(x)$ is the field of the beam falling on the prism base, r_{21} is the Fresnel coefficient of the reflection on the prism–air boundary, $D^+(x) = D_a^+(x) + D_b^+(x)$ is the SPP field component re-radiated into the prism (*a* for the free surface, *b* for the film), and the direction of the SPP propagation is chosen as the positive direction of the *x*-axis.

Unlike the Yeatman work, in our experiment, the field intensity of the incident radiation has the form of the Gaussian beam $E(x) = E_0 \exp[-(x - x_0)^2/w^2]$, where E_0 is the field amplitude in the center of the beam, x_0 is the center of the beam, and *w* is the half width of the beam. As a consequence, for the region ($x > 0$), in the reflected radiation there is a shift in the position of the maximum of the Gaussian beam towards the propagation of the SPPs, proportional to the efficiency of their generation (Figure 8b). We observed a similar phenomenon in the experiment.

(**a**)　　　　　　　　　　　　　　　　　　　　　　　　　　　(**b**)
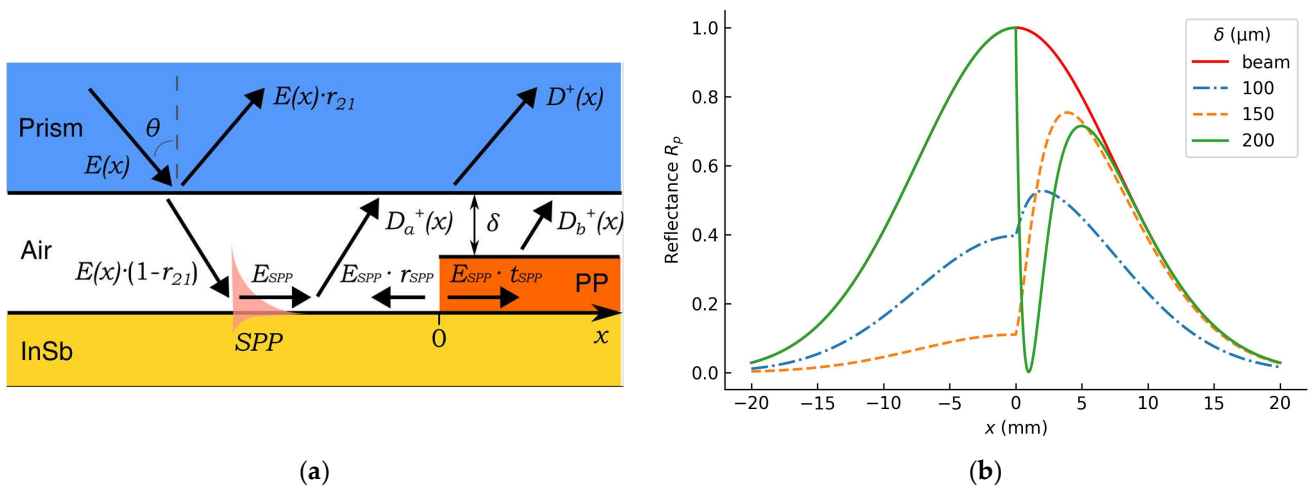
Figure 8. Simulation of SPR microscopy using the Yeatman model: (**a**) explanatory diagram for EM fields vectors; (**b**) calculated curves of the observed reflection coefficient $R(x)$ for a dielectric step under surface plasmon resonance conditions (InSb: $\varepsilon = -18.52 + 3.03i$, prism: $n = 1.5$; PP tape: $n = 1.5$, thickness 20 μm, $\lambda = 197$ μm).

For the free surface ($x < 0$), Yeatman assumed that the reflection of SPPs (r_{SPP}) from the dielectric step was negligible; so, the resulting field for $x < 0$ did not depend on the presence of film in the area $x > 0$. However, in the experiment, we observed that the incident Gaussian beam divided into the sum of two Gaussian beams, the maxima of which shifted away from the film boundary as the gap δ decreased. This indicates that the reflection of the THz SPPs from the film boundary (dielectric step) is substantial. Therefore, normalizing images of the reflected beams to the profile of the incident beam would lead to an error; so, the images and profiles of the beam sections in Figures 6 and 7 are given without such normalization.

To assess the efficiency of SPPs generation on the InSb surface, we summed the signal of the reflected part of the beam over the film (zone B) and without it (zone A) at different δ and normalized this sum to the maximum total signal reached at $\delta = 375$ μm for zones A and B, respectively. The $R(\delta)$ dependencies corresponding to the zones A (blue curve) and B (black curve) are shown in Figure 9. For comparison, the figure shows the red curve, which corresponds to the integral signal from the matrix receiver for the case of the THz beam illuminating the completely free InSb surface (see Figure 4). It can be seen that over zone A, the resonance efficiency is significantly weaker, but the position of the minimum of the resonance dip remains almost unchanged. This fact makes it possible to assert that the presence of a dip in the blue curve is mainly due to the generation of SPPs on the free section of the InSb surface (zone A), and the decrease in the efficiency of generation is caused, as mentioned earlier, by the propagation of the SPPs from the free InSb surface to the coated InSb area.

In the case of recording the distribution of intensity of the beam reflected from the area of the InSb surface with the PP film (zone B), the minimum of the resonance dip shifts on the $R(\delta)$ graph to the area of smaller gaps (black curve on Figure 9); this is due to the shifting of the resonance dip to the region of smaller gaps for the InSb with PP film and the smaller penetration depth of the SPPs' field into the air in the case of the application of the dielectric coating on the surface supporting the SPPs [30–32].

Thus, in the SPR microscopy method, the distribution of intensity in the reflected beam of the THz radiation makes it possible to distinguish areas of the InSb surface free from the 20 μm thick PP film from areas with such coating. The localization of the boundary between the areas with and without the film is most possible upon analysis of the $R(x)$ dependence measured with the maximum efficiency of SPP generation on the film-free

area (red curve in Figure 9): the film boundary corresponds to the $R(x)$ curve with higher reflectivity in zone B.
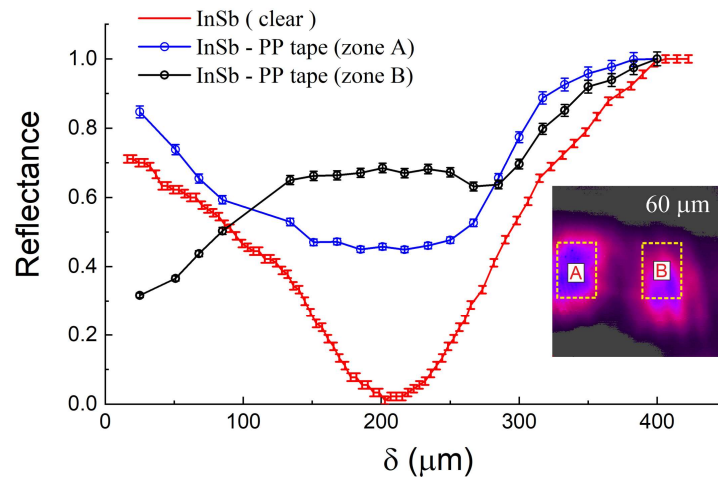
Figure 9. Reflectance vs. air gap measured for the InSb plate: red line—only the bare surface of InSb is illuminated (Figure 4); blue line—the signal summed over zone A (without PP film); black line—over zone B (with PP film). The inset shows part of Figure 6 with the marked zones.

3.3. Localization of Graphene Coating on the InSb Surface

In order to explore the possibilities of the SPR microscopy method for the study of thinner films, we applied a graphene strip, 6 mm wide and 35 nm thick, onto part of the InSb surface (Figure 10).
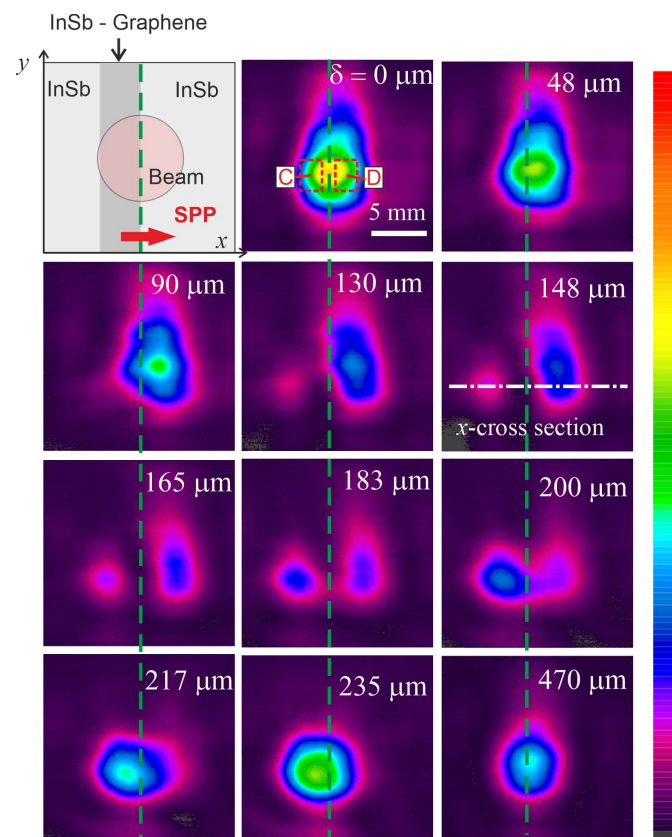
Figure 10. Images of the reflected beams vs. gap measured for the InSb plate, half of which was covered with a graphene layer 35 nm thick. The incident angle θ was 42.1°.

For manufacturing the indium antimonide sample coated with a thin graphene film we used composite inks, which include graphene flakes, and conductive polymer PE-DOT:PSS (Poly 3,4-ethylenedioxythiophene/polystyrenesulfonate) doped with ethylene glycol (Gr:PPS) [33]. This composite demonstrates a sheet resistance of ~$5 \cdot 10^3$ Ohm/sq [34]. An ethanol–water (70:30) suspension with a graphene content of 1 mg/mL was created for the experiments. A graphene structure of a few layers was created from the inks applied onto an InSb substrate by means of the 2D Dimatix FUJIFILM DMP-2831 jet printer. The optimal parameters of the printing process were a distance between the nozzles of 20 μm, a substrate temperature of 60 °C, and a drying time between printing the layers of 20 s.

The graphene layer thickness estimated from the spectrum of X-ray fluorescence with the electron microscope Hitachi S-3400N with the INCA element analysis module was 35 nm.

Figure 10 presents images of the intensity distribution in the cross-section of the THz radiation beam output from the ATR prism in the presence of the graphene strip on the surface of the InSb. In these images, there are no interference fringes observed in the case of a much thicker PP coating on the surface of the semiconductor (Section 3.2). In the images obtained at $\delta = 130-200$ μm, we also identified two zones: zone D, in the beam part corresponding to the free surface of the InSb, and zone C, in the beam part corresponding to the InSb surface covered with the graphene strip. Figure 11 shows profiles of the cross-sections of the intensity of these images along the *x*-axis. As δ increases, the cross-sections feature a decrease in the intensity of the reflected radiation in both zones, due to the generation of SPPs on the relevant parts of the sample's surface. However, since the generation of SPPs at these sites has varying efficiency, the maximum observed at $\delta = 0$ μm is divided into two smaller maxima. At 166 μm, the efficiency of SPPs generation on the graphene-covered surface reaches a maximum, as evidenced by the minimum intensity value in zone C. Further increasing of the air gap leads to a decrease in the efficiency of SPPs generation above the graphene-covered surface, which is accompanied by an increase in radiation intensity in zone C and a further increase in the efficiency of SPPs generation on the free surface of the InSb, which is confirmed by the continuing reduction in radiation intensity in zone D. At 235 μm, the efficiency of SPPs generation on the surface with the graphene layer attains its maximum value, as indicated by the minimum intensity value in zone D. A further increase of the gap is accompanied by a decrease in the efficiency of SPPs generation both on the free surface of the semiconductor and on its part with the graphene layer. This is confirmed by the higher illumination of both zones (C and D) of the matrix detector. This increase in illumination gradually leads to the merging of both maxima into one when the ATR prism base is beyond the SPP field ($\delta > 300$ μm). As with the PP film, some shift of the maxima is due to the SPP transition from one area to the other and the contribution of the SPP field to the radiation reflected from the prism base.

As with the PP film, the boundary of the graphene strip can best be localized from an analysis of the $R(x)$ dependence measured at the maximum efficiency of SPP generation on the film-free part (green curve in Figure 12 at 235 μm). The edge of the film corresponds to the curve $R(x)$ kink, with an increase in the reflectance in zone D (at 235 μm).

The change in the intensity of the reflected THz radiation can be seen more clearly in Figure 11, which shows the normalized dependencies for signals integrated over regions C and D (on Figure 10) on the gap size. The normalization was performed at the maximum value of the integral signal at $\delta = 470$ μm. For comparison, Figure 12 also shows the $R(\delta)$ graph over the fully free surface of the InSb (Figure 4). As with the film, the intensity of the reflected beam portion over the uncovered graphene surface of the InSb (zone D) has a minimum in the $R(\delta)$ dependence at the same gap ($\delta \approx 210$ μm) as at the illumination of the fully free surface of the InSb. The only difference is the depth of the resonance dip, which indicates the spread of the SPPs from the graphene-coated area to the area without such coating. In the case of the reflection of the beam from the graphene-coated area (zone C), the $R(\delta)$ dip shifts to the area of smaller gaps ($\delta \approx 150$ μm), due to the already mentioned reduction in the penetration depth of the SPP field into the air after application of the dielectric coating to the SPPs' guiding surface. Therefore, the InSb surface zones with and

without the thin graphene film can also be differentiated from the shift of the resonance curves in the $R(\delta)$ graph relative to the reference resonance curve over the completely uncovered area of the InSb. The value of the shift depends on the optical constants of the film and its thickness. For the 35 nm thick graphene coating we used, the shift in δ was about 60 μm, which is enough for the separation of the zones and for finding the boundary between them.
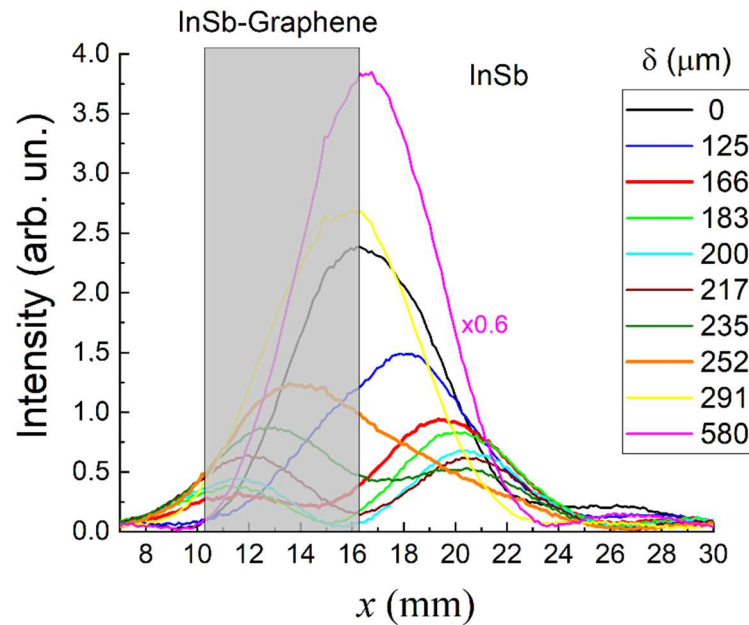

Figure 11. Cross-sections of the intensity profiles (see Figure 10) along the *x*-direction at different air gaps δ. For illustrative purpose, the cross-section intensity for δ = 580 μm was multiplied by 0.6.
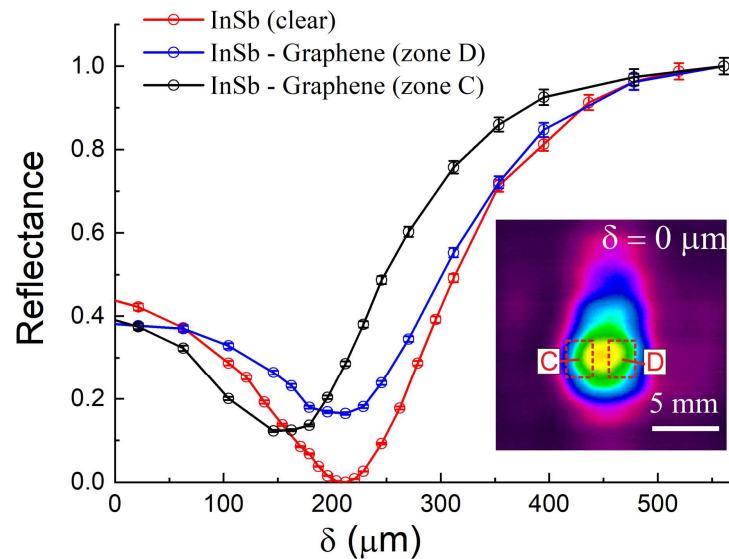
Figure 12. Reflectance vs. air gap, measured for the InSb plate: red line—only the bare InSb surface is illuminated (Figure 4); blue line—signal summed over zone D (without film); black line—signal summed over zone C (with film). The inset shows part of Figure 10 with the marked zones.

4. Conclusions

The surface plasmon (SP) microscopy method was successfully demonstrated in the terahertz (THz) frequency range. It was established that this microscopy technique can be utilized for investigating thin dielectric layers on flat semiconductor surfaces, provided

that the plasma frequency of the semiconductor is slightly different from the frequency of the probing radiation. This condition ensures that the propagation length of the surface plasmon polaritons (SPPs) is comparable to the wavelength of the radiation. By employing a coherent radiation from the Novosibirsk free electron laser (with a wavelength of approximately 197 μm) and the Otto configuration for exciting SPPs, we obtained images of a polypropylene coating 20 μm thick and a graphene coating 35 nm thick on a flat indium antimonide (InSb) substrate, varying the air gap between the attenuated total reflection (ATR) prism and the surface under investigation.

We have determined that the most effective approach for localizing the boundary between coated and uncoated regions is by identifying the point of reflection coefficient kink in the probing radiation beam that illuminates the boundary under optimal SPPs generation conditions on the uncoated region. When the coating thickness is small compared with the wavelength and the depth of the SPP field penetration into air, differentiation between the semiconductor surface areas with and without coating is also possible via a comparison of the optimal gap values between the free and coated InSb surfaces with respect to the optimal gap corresponding to the plasmon resonance on the completely uncoated InSb surface.

References

1. Peiponen, K.-E.; Zeitler, J.A.; Kuwata-Gonokami, M. *Terahertz Spectroscopy and Imaging*; Springer: Berlin/Heidelberg, Germany; New York, NY, USA, 2013; ISBN 978-3-642-29563-8.
2. Cherkasova, O.P.; Serdyukov, D.S.; Ratushnyak, A.S.; Nemova, E.F.; Kozlov, E.N.; Shidlovskii, Y.V.; Zaytsev, K.I.; Tuchin, V.V. Effects of Terahertz Radiation on Living Cells: A Review. *Opt. Spectrosc.* **2020**, *128*, 855–866. [CrossRef]
3. Chernomyrdin, N.V.; Musina, G.R.; Nikitin, P.V.; Dolganova, I.N.; Kucheryavenko, A.S.; Alekseeva, A.I.; Wang, Y.; Xu, D.; Shi, Q.; Tuchin, V.V.; et al. Terahertz Technology in Intraoperative Neurodiagnostics: A Review. *Opto Electron. Adv.* **2022**, *6*, 220071. [CrossRef]
4. Costa, F.B.; Machado, M.A.; Bonfait, G.J.; Vieira, P.; Santos, T.G. Continuous Wave Terahertz Imaging for NDT: Fundamentals and Experimental Validation. *Measurement* **2021**, *172*, 108904. [CrossRef]
5. Cosentino, A. Terahertz and Cultural Heritage Science: Examination of Art and Archaeology. *Technologies* **2016**, *4*, 6. [CrossRef]
6. Wang, J.; Ando, M.; Nagata, H.; Yoshida, S.; Sakai, K.; Kiwa, T. Multifunctional Terahertz Microscopy for Biochemical and Chemical Imaging and Sensing. *Biosens. Bioelectron.* **2023**, *220*, 114901. [CrossRef]

7. Moon, K.; Do, Y.; Park, H.; Kim, J.; Kang, H.; Lee, G.; Lim, J.-H.; Kim, J.-W.; Han, H. Computed Terahertz Near-Field Mapping of Molecular Resonances of Lactose Stereo-Isomer Impurities with Sub-Attomole Sensitivity. *Sci. Rep.* **2019**, *9*, 16915. [CrossRef]
8. Chen, S.; Bylinkin, A.; Wang, Z.; Schnell, M.; Chandan, G.; Li, P.; Nikitin, A.Y.; Law, S.; Hillenbrand, R. Real-Space Nanoimaging of THz Polaritons in the Topological Insulator Bi_2Se_3. *Nat. Commun.* **2022**, *13*, 1374. [CrossRef] [PubMed]
9. Chernomyrdin, N.V.; Skorobogatiy, M.; Ponomarev, D.S.; Bukin, V.V.; Tuchin, V.V.; Zaytsev, K.I. Terahertz Solid Immersion Microscopy: Recent Achievements and Challenges. *Appl. Phys. Lett.* **2022**, *120*, 110501. [CrossRef]
10. Ning, W.; Hu, N.; Xu, P.; Song, Y.; Li, Y. Performance Comparison of Different Deconvolution Methods on 2D Terahertz Imaging. *Microw. Opt. Technol. Lett.* **2023**, 1–6. [CrossRef]
11. Guerboukha, H.; Cao, Y.; Nallappan, K.; Skorobogatiy, M. Super-Resolution Orthogonal Deterministic Imaging Technique for Terahertz Subwavelength Microscopy. *ACS Photonics* **2020**, *7*, 1866–1875. [CrossRef]
12. Khasanov, I.S.; Zykova, L.A. Terahertz Ghost Imaging and Surface Plasmon Resonance Microscopy: Analysis of Factors Affecting the Image Quality. In Proceedings of the Fourth International Conference on Terahertz and Microwave Radiation: Generation, Detection, and Applications, Tomsk, Russian, 24–26 August 2020; Romanovskii, O.A., Kistenev, Y.V., Eds.; SPIE: Tomsk, Russian, 2020; p. 54.
13. Ma, D.; Zhao, J.; Wang, D.; Lin, H.; Rong, L.; Wang, Y.; Lin, S. Full-Field Super-Resolution Terahertz Imaging Based on Rotating Coherent Scattering Microscopy. *Appl. Sci.* **2023**, *13*, 982. [CrossRef]
14. Yeatman, E.; Ash, E.A. Surface Plasmon Microscopy. *Electron. Lett.* **1987**, *23*, 1091. [CrossRef]
15. Rothenhäusler, B.; Knoll, W. Surface–Plasmon Microscopy. *Nature* **1988**, *332*, 615–617. [CrossRef]
16. Gerasimov, V.V.; Knyazev, B.A.; Kotelnikov, I.A.; Nikitin, A.K.; Cherkassky, V.S.; Kulipanov, G.N.; Zhizhin, G.N. Surface Plasmon Polaritons Launched Using a Terahertz Free-Electron Laser: Propagation along a Gold–ZnS–Air Interface and Decoupling to Free Waves at the Surface Edge. *J. Opt. Soc. Am. B* **2013**, *30*, 2182–2190. [CrossRef]
17. Liu, Z. (Ed.) *Plasmonics and Super-Resolution Imaging*; Pan Stanford Publishing: Singapore, 2017; ISBN 978-981-4669-91-7.
18. Maier, S.A. *Plasmonics: Fundamentals and Applications*; Springer: New York, NY, USA, 2007; ISBN 978-0-387-33150-8.
19. Teng, Y.-Y.; Stern, E.A. Plasma Radiation from Metal Grating Surfaces. *Phys. Rev. Lett.* **1967**, *19*, 511–514. [CrossRef]
20. Raether, H. *Surface Plasmons on Smooth and Rough Surfaces and on Gratings*; Springer Tracts in Modern Physics; Springer: Berlin/Heidelberg, Germany, 1988; Volume 111, ISBN 978-3-540-17363-2.
21. Harris, R.D.; Wilkinson, J.S. Waveguide Surface Plasmon Resonance Sensors. *Sens. Actuators B Chem.* **1995**, *29*, 261–267. [CrossRef]
22. Otto, A. Excitation of Nonradiative Surface Plasma Waves in Silver by the Method of Frustrated Total Reflection. *Z. Phys. A Hadron. Nucl.* **1968**, *216*, 398–410. [CrossRef]
23. Kretschmann, E.; Raether, H. Notizen: Radiative Decay of Non Radiative Surface Plasmons Excited by Light. *Z. Nat. A* **1968**, *23*, 2135–2136. [CrossRef]
24. Shibayama, J.; Mitsutake, K.; Yamauchi, J.; Nakano, H. Kretschmann- and Otto-Type Surface Plasmon Resonance Waveguide Sensors in the Terahertz Regime. *Microw. Opt. Technol. Lett.* **2021**, *63*, 103–106. [CrossRef]
25. Yang, Y.; Zhai, C.; Zeng, Q.; Khan, A.L.; Yu, H. Quantitative Amplitude and Phase Imaging with Interferometric Plasmonic Microscopy. *ACS Nano* **2019**, *13*, 13595–13601. [CrossRef]
26. Nikitin, A.K.; Gerasimov, V.V.; Knyazev, B.A.; Lien, N.T.H.; Trang, T.T. Control of the Conducting Surface by Terahertz Surface Electromagnetic Waves. *J. Phys. Conf. Ser.* **2020**, *1636*, 012036. [CrossRef]
27. Vinokurov, N.A.; Shevchenko, O.A. Free electron lasers and their development at the Budker Institute of Nuclear Physics, SB RAS. *Physics-Uspekhi* **2018**, *61*, 435–448. [CrossRef]
28. Anisimov, A.V.; Khasanov, I.S. Algorithm for Optical Characterization of Dielectric Gradient Index Nanofilm by Surface Plasmon Resonance Spectroscopy. *J. Phys. Conf. Ser.* **2021**, *2091*, 012067. [CrossRef]
29. Yeatman, E.M. Resolution and Sensitivity in Surface Plasmon Microscopy and Sensing. *Biosens. Bioelectron.* **1996**, *11*, 635–649. [CrossRef]
30. Bell, R.J.; Alexander, R.W.; Ward, C.A.; Tyler, I.L. Introductory theory for surface electromagnetic wave spectroscopy. *Surf. Sci.* **1975**, *48*, 253–287. [CrossRef]
31. Raether, H. Surface plasma oscillations and their applications. *Phys. Thin Film.* **1977**, *9*, 145–261.
32. Pockrand, I. Surface plasma oscillations at silver surfaces with transparent and absorbing coatings. *Surf. Sci.* **1978**, *72*, 577–588. [CrossRef]
33. Yakimchuk, E.A.; Soots, R.A.; Kotin, I.A.; Antonova, I.V. 2D printed graphene conductive layers with high carrier mobility. *Curr. Appl. Phys.* **2017**, *17*, 1655–1661. [CrossRef]
34. Antonova, I.V.; Shavelkina, M.B.; Ivanov, A.I.; Poteryaev, D.A.; Nebogatikova, N.A.; Buzmakova, A.A.; Soots, R.A.; Katarzhis, V.A. Graphene: Hexagonal Boron Nitride Composite Films with Low-Resistance for Flexible Electronics. *Nanomaterials* **2022**, *12*, 1703. [CrossRef]